Solid-state NMR of endohedral hydrogen–fullerene complexes

M. Carravetta,[a] A. Danquigny,[a] S. Mamone,[a] F. Cuda,[a] O. G. Johannessen,[a] I. Heinmaa,[b] K. Panesar,[c] R. Stern,[b] M. C. Grossel,[a] A. J. Horsewill,[c] A. Samoson,[b] M. Murata,[d] Y. Murata,[d] K. Komatsu[d] and M. H. Levitt*[a]

Received 9th May 2007, Accepted 14th June 2007
First published as an Advance Article on the web 12th July 2007
DOI: 10.1039/b707075f

We present an overview of solid-state NMR studies of endohedral H_2-fullerene complexes, including ^{1}H and ^{13}C NMR spectra, ^{1}H and ^{13}C spin relaxation studies, and the results of ^{1}H dipole–dipole recoupling experiments. The available data involves three different endohedral H_2-fullerene complexes, studied over a wide range of temperatures and applied magnetic fields. The symmetry of the cage influences strongly the motionally-averaged nuclear spin interactions of the endohedral H_2 species, as well as its spin relaxation behaviour. In addition, the non-bonding interactions between fullerene cages are influenced by the presence of endohedral hydrogen molecules. The review also presents several pieces of experimental data which are not yet understood, one example being the structured ^{1}H NMR lineshapes of endohedral H_2 molecules trapped in highly symmetric cages at cryogenic temperatures. This review demonstrates the richness of NMR phenomena displayed by H_2-fullerene complexes, especially in the cryogenic regime.

1. Introduction

The symmetrical cage of 60 carbon atoms in fullerene encloses a cavity with a diameter of approximately 700 pm. This void space has been a magnet for synthetic chemists and chemical physicists, who have succeeded in occupying it with a wide variety of atoms and small molecules to form a range of extraordinary endohedral complexes.[1–19] Notable achievements include the trapping of helium atoms, to produce the only chemical compounds of helium that are stable under ordinary conditions,[2–6] and the trapping of single nitrogen and phosphorus atoms, to generate paramagnetic complexes with extraordinarily long electron spin coherence lifetimes.[13–15]

A particularly fascinating range of compounds is formed when dihydrogen molecules are trapped inside the cage.[5,7–12] These complexes cannot be formed directly by combining fullerene and hydrogen, since the hydrogen molecule is too large to pass through the gaps between the carbon atoms, even under extreme conditions. Instead, the synthesis of these complexes involves heroic multistage syntheses. A series of controlled chemical reactions opens orifices in the cage, leading to *open-cage fullerenes*.[7,10,20–22] The hydrogen molecules are forced through the orifices using conditions of high temperature and pressure, generating endohedral dihydrogen–fullerene complexes which are stable under ordinary conditions. The endohedral hydrogen molecules are readily identified by solution NMR, since the magnetic shielding effect of the cage leads to unusual chemical shifts, which are often negative.[5,7–12]

The first compound of this type was synthesized by the group of Rubin.[5] However the yield of the endohedral complex was less than 10%. The group of Komatsu used a different synthetic route, and achieved near-100% yield for the endohedral complex of dihydrogen with aza-thia-open-cage-fullerene (ATOCF),[8] which contains a 13-membered orifice (H_2@ATOCF, see Fig. 1a). The orifice was closed by a further sequence of chemical reactions, with the dihydrogen molecule still inside, leading to the symmetrical complex H_2@C_{60}.[9,10] The physical properties of C_{60} and H_2@C_{60} are slightly different, allowing their separation by high-pressure liquid chromatography.[9] An additional range of compounds was synthesized by subjecting the closed fullerene cage to exohedral modifications, without releasing the hydrogen.[10]

The behaviour of the trapped dihydrogen molecules is of great interest. Dihydrogen exhibits some extraordinary quantum properties, even at relatively high temperature, because of

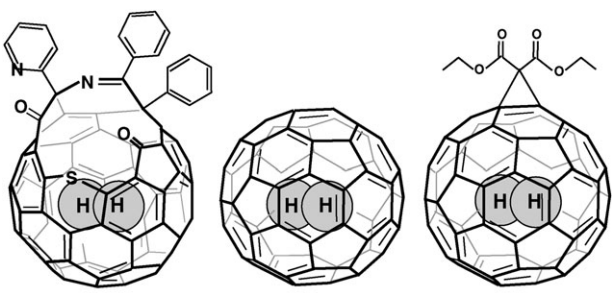

Fig. 1 Molecular structures of the compounds studied in this work: **I**: H_2@ATOCF (aza-thia-open-cage-fullerene); **II**: H_2@C60; **III**: H2@di(ethoxycarbonyl)methanofullerene.

[a] *School of Chemistry, University of Southampton, Southampton, UK SO17 1BJ. E-mail: mhl@soton.ac.uk*
[b] *National Institute of Chemical Physics and Biophysics, Tallinn, 12618, Estonia*
[c] *Department of Physics, University of Nottingham, UK*
[d] *Kyoto University, Kyoto, 611-0011, Japan*

its very simple molecular structure and low molecular moment of inertia. Since the spin-1/2 proton nuclei are fermions, the Pauli principle requires that the total quantum state is antisymmetric with respect to nuclear exchange. Furthermore, only the lowest electronic and vibrational states, which are symmetric with respect to nuclear exchange, are populated at room temperature. As a result, the rotational quantum state must have the opposite exchange parity to the nuclear spin states. This leads to the phenomenon of nuclear spin isomers. The *para*-hydrogen spin isomer is comprised of the rotational states with even rotational quantum numbers J and a total nuclear spin of zero. The *ortho*-hydrogen spin isomer is comprised of the odd-J rotational states and a total nuclear spin of one. The nuclear spin isomers only interconvert very slowly in the absence of a catalyst, and in most conditions behave essentially as separate physical substances.[23–25]

The confined hydrogen molecules display translational quantization in addition to their rotational quantization. To a first approximation, the translational motion of the endohedral H_2 molecule resembles that of a quantum particle trapped inside a 3-D spherical container—a case which may be solved exactly.[26] However, the realistic quantum motion of the endohedral H_2 molecules is also strongly influenced by the coupling between the translational and rotational motion. This translation–rotation coupling depends on the symmetry of the cage. These systems therefore provide unique opportunities for studying the behaviour of quantum rotors under close confinement, and for testing theories of quantum motion.

Endohedral hydrogen–fullerene complexes have been studied by the following spectroscopic tools: solution NMR,[5,7–12] mass spectrometry,[10] ultraviolet/visible spectroscopy,[10] Raman spectroscopy,[27] and solid-state NMR.[28,29]

Solution-state ^{1}H NMR is usually employed for the primary characterization of these complexes, since the endohedral protons have unusual chemical shifts. For example, the insertion yield of the dihydrogen is usually determined by comparing the integrals of the peaks from the endohedral and exohedral protons. In addition, the ^{13}C chemical shift of the fullerene atoms is slightly influenced by the presence of a endohedral H_2 molecule.[9]

Solution NMR has also been used to study the relaxation of the endohedral protons.[12] The proton T_1 displays an unusual T_1-maximum with respect to the temperature. Dissolved dihydrogen molecules which are not trapped in cages exhibit a similar T_1-maximum, which suggests a common physical mechanism.[12]

Raman spectroscopy of the complexes is difficult, due to the strong fluorescence of the fullerene cages. Nevertheless, it is possible to detect the vibrations of the endohedral hydrogen molecules.[27]

This review is concerned with the solid-state NMR of endohedral hydrogen–fullerene complexes. Unlike solution NMR, solid-state NMR can access a wide range of temperatures from the cryogenic regime to well above room temperature. A variety of experimental techniques are available, which provide information on both the timescale and anisotropy of the quantum rotation, as well as the behaviour of the cages themselves, and the interactions between the cages and the confined rotors.

There have been several solid-state NMR studies of confined molecules, which predate the subject of this review. These include NMR experiments on hydrogen molecules trapped in inert matrices[30] and on *interstitial* hydrogen–fullerene complexes, in which the hydrogen molecules are trapped *between* the fullerene cages, rather than inside them.[31,32] However, the interstitial complexes are relatively difficult to handle. They are only stable in a hydrogen atmosphere, which hinders the use of magic-angle-spinning NMR, which is usually necessary for obtaining high-resolution NMR spectra. Furthermore, the environment of the confined molecules cannot be manipulated as readily as for the endohedral complexes. Nevertheless, the elegant work by Tomaselli and co-workers on interstitial H_2-fullerene complexes[31,32] has inspired much of the research described in this article.

^{1}H NMR can only provide information on the *ortho* spin isomer, since the *para* spin isomer has zero total nuclear spin and does not give an NMR signal. This restriction may be avoided by studying endohedral HD or D_2–fullerene complexes. However, at the time of writing, there have been no solid-state NMR studies of these species. All the ^{1}H NMR data presented in this article therefore refers to *ortho*-hydrogen molecules trapped inside fullerene cages. This is the case even at low temperature, where complete thermal equilibrium would lead to depletion of *ortho*-hydrogen in favour of the NMR-silent $J = 0$ *para*-hydrogen state. In practice, such depletion is not observed, presumably because the *ortho–para* interconversion rate is negligible.[29]

Another point of interest is the motion of the fullerene cages themselves, and how this motion is influenced by the presence of the endohedral molecules. The behaviour of the fullerene cages may be studied by ^{13}C NMR. There is a rich source of literature on the solid-state dynamics of C_{60} cages, as revealed by ^{13}C NMR.[32–35] C_{60} undergoes a phase transition at around 260 K, with a sharp decrease in the lattice constant associated with the establishment of an order in the preferential relative orientation of the fullerenes.[36] The glass transition temperature is around 130 K, above which the cages rotate rapidly and almost isotropically on the NMR timescale.[32–35] Evidence is presented below that the endohedral H_2 molecules influence the C_{60} cage dynamics significantly.

The detailed study of endohedral H_2-fullerene complexes by solid-state NMR is also motivated by a wider issue. In recent years, there has been a great deal of interest in improving the signal strength of NMR spectroscopy. A variety of approaches have been proposed, most of which involve generating enhanced non-equilibrium nuclear spin magnetization by methods including optical pumping,[37] microwave irradiation of unpaired electron dopants,[38,39] chemical reactions of *para*hydrogen,[24,25] or temperature jumps in the cryogenic regime to induce the Haupt effect.[40,41] A relatively straightforward and general method for increasing the nuclear spin magnetization is simply to reduce the sample temperature. For example, the nuclear spin magnetization achieved in thermal equilibrium at 4 K is about 60 times greater than the room temperature magnetization. However, to exploit this large signal strength, at least two obstacles must be overcome. First, it is necessary to overcome the technical difficulties of performing high-resolution solid-state NMR (including magic-angle-spinning

NMR) in the cryogenic regime. Second, one must circumvent the very slow spin–lattice relaxation time constants which are typical of many substances in the cryogenic regime. An enhancement in the thermal equilibrium spin magnetization by a factor of 30 would not be particularly useful if the enhanced magnetization takes many hours to build up.

A great deal of progress has now been made in developing high-resolution NMR equipment capable of cryogenic operation, including fast magic-angle-spinning capability.[42–44] At the time of writing, this equipment is too unstable to be used for multiple-pulse NMR experiments, but this situation is likely to improve within the next few years. Nevertheless, the obstacle presented by slow spin–lattice relaxation will still remain. This is where the endohedral hydrogen–fullerene complexes come in. The complete rotational freedom of the trapped hydrogen molecules, and their low moment of inertia, ensure rapid molecular motion even in the cryogenic regime. As shown below, some endohedral complexes display very rapid nuclear spin–lattice relaxation at temperatures below 50 K and can serve as relaxation sinks for the immediate molecular environment. In the future, such complexes could be functionalized so as to bind to particular molecular sites in, for example, a protein. The proton magnetization of the neighbouring molecular region should be strongly enhanced by spin-diffusion to the rapidly-relaxing confined quantum rotor. The endohedral complex should serve as a cryogenic relaxation agent, or *cryorelaxor*, which "lights up" the NMR signals of targeted regions in a large biomolecule.

The NMR results shown in the rest of this review were collected as part of a general effort to understand the motion of hydrogen molecules trapped inside fullerene cages, and the impact of that motion on nuclear spin–lattice relaxation, especially in the cryogenic regime. Much of these data have not been published before, and awaits a detailed analysis.

The remainder of this article is structured as follows: section 2 provides details on the NMR methods and pulse sequences used to acquire the experimental data. Section 3 provides the relevant information about the samples, the NMR equipment and the experimental conditions under which the data were acquired. The following sections present the experimental NMR data themselves, organized by compound.

2. Solid-state NMR methods

Solid-state NMR may be performed either on static samples, or on samples rotating rapidly at the "magic angle" (arctan $\sqrt{2} \cong 54.74°$) with respect to the applied magnetic field.[45–48]

The NMR of static samples may be performed using readily-available equipment at temperatures down to around 2 K, and a wide variety of magnetic field strengths. However, static NMR usually provides broad resonance lines, suffers from poor sensitivity, and cannot distinguish between the resonances of different chemical sites.

Magic-angle-spinning (MAS) averages out anisotropic nuclear spin interactions, leading to chemical site resolution and improved signal strength.[45–48] However, MAS is subject to technical limitations, especially in the cryogenic regime. At the moment, the lowest accessible temperature for MAS-NMR is around 15 K.[29,44] Some of the more sophisticated MAS-NMR experiments require a very stable spinning frequency, which at the time of writing may only be achieved at sample temperatures above around 120 K. Most of the low-temperature results presented in this article were obtained under static conditions, while most of the high-temperature data was obtained using magic-angle spinning.

The pulse sequences used in this work are sketched in Fig. 2 and 3. Each pulse sequence is made up of radio-frequency (rf) pulses and time intervals, followed by acquisition of the NMR signal (the free induction decay, or FID). In the following discussion, the rf pulses are indicated using the notation β_ϕ, where β is the flip angle and ϕ is the phase, both usually expressed in degrees.[48]

A. Pulse sequences for ^{1}H NMR

The pulse sequences in Fig. 2 are used for observing the abundant ^{1}H nuclei.

(a) One-pulse sequence. A single 90_0 pulse followed by the acquisition of the NMR signal, *i.e.* 90_0-Acq. Fourier transformation of the NMR signal yields the ^{1}H NMR spectrum. The main limitation of this pulse sequence is that, for technical reasons, the signal acquisition cannot start immediately after the pulse. This leads to signal distortions in the case of rapidly decaying NMR signals. In such cases, spin echoes may be used (see below).

The ^{1}H NMR spectra of static powders are often broad and uninformative, due to the anisotropic dipole–dipole couplings.

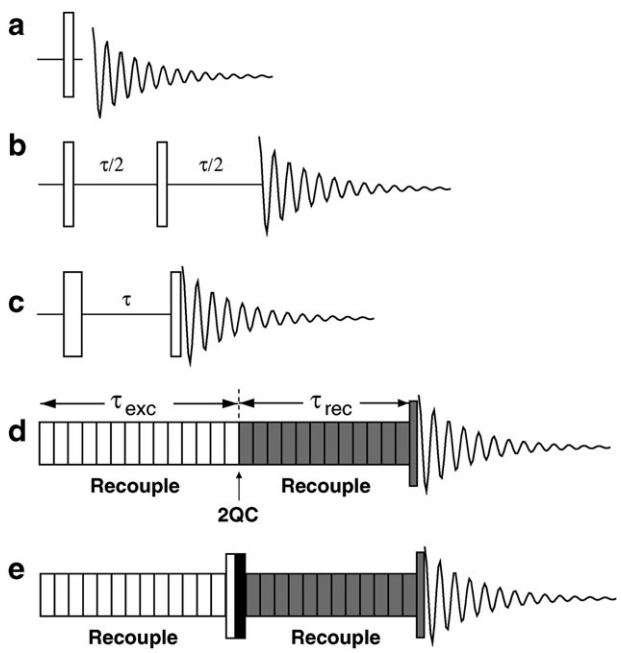

Fig. 2 Pulse sequences for solid-state ^{1}H NMR. Narrow rectangles denote 90° pulses; wide rectangles denote 180° pulses. (a) One-pulse sequence; (b) Solomon echo sequence, using two 90° pulses with a mutual phase shift of 90°; (c) inversion recovery sequence, for longitudinal relaxation measurements; (d) double-quantum recoupling sequence, for homonuclear dipole–dipole coupling estimations. The phases of the shaded pulse sequence elements are cycled in order to suppress signals not passing through double-quantum coherence; (e) pulse sequence used for spherical tensor analysis.

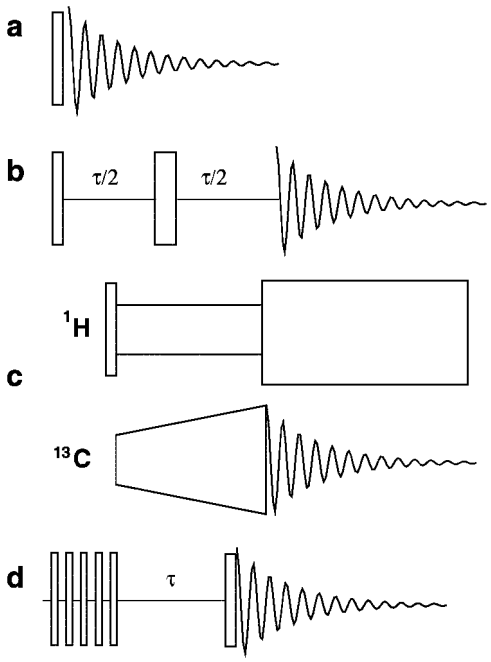

Fig. 3 Pulse sequences for solid-state ^{13}C NMR: (a) one-pulse sequence; (b) Carr–Purcell echo, using a 90° pulse followed by a 180° pulse; (c) ramped cross polarization sequence, to transfer polarization from ^{1}H to ^{13}C; (d) saturation-recovery, for longitudinal relaxation time measurements.

However, the samples described here sometimes display well-defined and informative static ^{1}H lineshapes in the cryogenic regime, due to the relative isolation of the endohedral H_2 molecules. These spectra often depend strongly on temperature, reflecting the distribution of the molecules between the available spatial quantum states.[29,31,32] If magic-angle spinning is used, the endohedral H_2 peaks become very narrow, even at low spinning frequencies, and split up into sideband patterns due to the intramolecular proton–proton dipolar coupling.[28,29]

(b) Solomon echo. $90_0 - \tau/2 - 90_{90} - \tau/2 -$ Acq.[49] This pulse sequence generates a spin echo if the sample is static (*i.e.* the sample is not rotating), and if the spin system consists of approximately isolated spin-1/2 pairs, which is the situation for the endohedral *ortho*-H_2 molecules. The second pulse reverses the rapid signal decay caused by the intra-pair dipole–dipole coupling, leading to a dipolar spin echo. Fourier transformation of the signal starting from the top of the echo leads to undistorted lineshapes. Signals from nuclei which participate in more complex dipole–dipole coupling networks do not form strong Solomon echoes, and are partially suppressed. This pulse sequence was used for monitoring the ^{1}H lineshapes of the endohedral H_2 molecules under static conditions at low temperature, while suppressing the signals from exohedral protons.

(c) Inversion-recovery (IR). $180_0 - \tau - 90_0 -$ Acq. The longitudinal magnetization is inverted by the first pulse, partially recovers through spin–lattice relaxation during the interval τ, and is converted into transverse magnetization by the second pulse. The NMR signal after the second pulse is monitored as a function of the recovery delay τ, in order to determine the spin–lattice relaxation time constant T_1.

(d) Dipolar recoupling. Magic-angle spinning averages out the anisotropic nuclear spin interactions, providing enhanced signal strength and chemical site selectivity. Despite these advantages, the suppression of the anisotropic spin interactions by MAS comprises a loss of important information. Fortunately, this information may often be recovered by applying radio-frequency pulse sequences that are synchronized with the sample rotation. This is called *recoupling*.[50–60] A set of symmetry-based design rules have been devised which allow the spectroscopist to control the type of spin interaction that is recoupled, and the type that is suppressed.[54–60]

The results shown in this article were obtained using symmetry-based recoupling sequences of the RN_n^v type.[56] The symmetry numbers N, n and v control the timing and phases of the pulses according to standard formulae.[54–60] To obtain the results shown below, these symmetry numbers were chosen to achieve double-quantum homonuclear dipolar recoupling under MAS. The recoupling sequences create correlated two-spin states, called double-quantum (DQ) coherences, which originate from the dipole–dipole interactions between like spins. The double-quantum coherences are excited by a recoupling sequence of duration τ_{reconv}, and then reconverted back into observable magnetization by a second recoupling sequence of duration τ_{exc}. Signals that do not pass through double-quantum coherences are suppressed using a phase-cycling procedure.[48] This is called *double-quantum filtration* (DQF). For the samples discussed here, double-quantum filtration is particularly useful for suppressing the exohedral proton NMR signals.

In the present context, double-quantum recoupling is particularly useful for measuring the strength of the motionally averaged ^{1}H–^{1}H dipole–dipole interaction between the *ortho*-hydrogen protons, while taking advantage of the chemical shift resolution provided by MAS. In general, the endohedral ^{1}H–^{1}H coupling is finite because the rapid rotational motion of the H_2 inside the cage is not isotropic. The motionally-averaged dipole–dipole coupling constant is given in a semi-classical description by:

$$b = -\frac{\mu_0}{4\pi}\frac{\gamma_H^2\hbar}{r_{HH}^3}S_{HH}^2 \qquad (2.1)$$

where γ_H is the proton gyromagnetic ratio and r_{HH} is the ^{1}H–^{1}H distance. The order parameter S_{HH}^2 describes the anisotropy of the rotational motion. If this motion is assumed, for simplicity, to have cylindrical symmetry about a fixed molecular axis, the order parameter is given by

$$S_{HH}^2 = \left\langle \frac{1}{2}(3\cos^2\theta_{HH} - 1) \right\rangle \qquad (2.2)$$

where θ_{HH} is the angle between the ^{1}H–^{1}H vector and the symmetry axis.

The dipole–dipole coupling is estimated by following the amplitude of the double-quantum-filtered NMR signal as the durations of the excitation period τ_{exc} and/or reconversion

period τ_{rec} are changed. Two different procedures may be used: in the asymmetric protocol, τ_{exc} is changed while keeping τ_{rec} fixed. This procedure is most convenient for measuring large dipole–dipole couplings.[56] In the *constant-time* protocol, the intervals τ_{exc} and τ_{rec} change in opposite senses, while keeping $\tau_{exc} + \tau_{rec}$ fixed.[57,61,62] This procedure is most useful for estimating small dipole–dipole coupling constants.

(e) Spherical tensor analysis (STA). Double-quantum-filtered recoupling experiments are sufficient when the coupled spin system consists of isolated spin pairs. For larger spin systems, a more sophisticated approach called *spherical tensor analysis* is appropriate.[63] A detailed description of this procedure is beyond the scope of this article. Briefly, any component of nuclear spin order may be described using a set of spherical tensor operators. In the context of this work, it suffices to say that these objects are characterised by two numbers, a spin rank λ and a coherence order μ, such that $|\mu| \leq \lambda$. The STA experiment allows one to estimate the amplitude of spin order components with particular values of λ and μ at any point in the NMR pulse sequence. A system of N coupled spins-1/2 only supports spin order components for which $|\mu|$ and λ are both less than or equal to N. The presence of components with particular values of λ and μ therefore sets a lower limit on the number of nuclei involved in the nuclear spin order at any point in a NMR pulse sequence. A STA experiment can therefore establish the participation of intermolecular spin–spin interactions, by showing that spin order components exist with λ or $|\mu|$ exceeding the dimension of the molecular spin system. STA is an extension of the earlier "spin counting" experiments, which only exploit the quantum number μ.[64–67]

B. Pulse sequences for ^{13}C NMR

The ^{13}C pulse sequences used to obtain the results given in this paper are displayed in Fig. 3. Unless otherwise specified, it is assumed that proton decoupling is applied during the signal detection period. Most of the results shown in this paper were obtained using SPINAL-64 decoupling.[68]

(a) One-pulse sequence. 90_0 – Acq. This may be used to observe the ^{13}C magnetization both for static and rotating solids. In static powders, ^{13}C NMR spectra take the form of broad "powder patterns" which are determined by the chemical shift anisotropy (CSA). In the case of C_{60}, the ^{13}C peaks become narrow above a certain temperature, due to the rapid thermally-activated rotation of the fullerene cages, which averages out the CSA.[33–35] The static ^{13}C NMR lineshapes therefore allow study of the thermally-driven rotation of the fullerene cages in a solid. When MAS is used, the ^{13}C peaks become narrow and appear at the isotropic chemical shift positions. Spinning sidebands, induced by the CSA, may also appear.

(b) Carr-purcell echo. $90_0 - \tau/2 - 180_0 - \tau/2$ – Acq. The Carr-Purcell echo[69] is used to reverse the rapid signal decay caused by the CSA in static powders, or by poor magnetic field inhomogeneity.

(c) Cross-polarization (CP). The ^{13}C signal strength may be enhanced by exploiting the polarization of nearby proton nuclei, using amplitude-ramped Hartmann–Hahn cross-polarization.[70–72] This method also allows faster data acquisition than the one-pulse ^{13}C experiment, since the ^{1}H nuclei usually have much shorter T_1 values.

(d) Saturation-recovery (SR). Used for all T_1 measurements on ^{13}C, which are typically quite long.

3. Experimental

A. Samples

All endohedral H_2-fullerene complexes were prepared using the procedures described by Komatsu and coworkers[7–12] and have an endohedral H_2 insertion yield approaching $\sim$100%, as verified by ^{1}H and ^{13}C solution NMR, as well as MALDI-TOF mass-spectrometry. The compounds are stable in ordinary conditions, although we observed some degradation on prolonged exposure to bright light.

B. NMR equipment

In the following, experiments with sample temperatures above $\sim$100 K are referred to as "high-temperature" measurements, while "low-temperature", or cryogenic, NMR experiments involve temperatures between 2.5 and 100 K. "High-field" experiments indicate magnetic field strengths of 4.7 T and above, while "low-field" experiments involve magnetic fields below 4.7 T.

High-temperature MAS-NMR experiments were recorded in Southampton on Varian Infinity + spectrometers using 4 mm zirconia rotors in fields of 7.0 and 9.4 T. The room temperature T_1 measurements were performed under a nitrogen atmosphere, in order to minimize the interference in the T_1 measurements due to oxygen. The variable-temperature experiments were performed using nitrogen gas for bearing and drive and a cold nitrogen flow to cool the sample. The sample temperature was estimated using the ^{207}Pb resonance of lead nitrate as a reference, under comparable conditions.[73–75]

The high-field cryogenic solid-state NMR experiments were performed in Tallinn at fields of 4.7, 8.5 and 14.1 T. The temperature was monitored using a calibrated Lakeshore Cernox sensor, with an accuracy of at least 0.1 K, placed in the proximity of the sample. The cooling was achieved by a controlled flow of helium into the cryostat. For cryogenic static experiments, the sample was placed in a pyrex tube with an outer diameter of 2.5 mm. For cryogenic MAS (cryoMAS) experiments, the sample was placed in a 1.8 mm SiN rotor. Regulated flows of helium gas were used for the gas bearings and to spin the sample at rotation frequencies up to 20 kHz.[44]

The low-field relaxion measurements were performed in Nottingham on a field cycling NMR instrument, with an observation field of 0.74 T.[76] The samples were contained in 5 mm NMR tubes and the temperature was measured with a calibrated Lakeshore Cernox sensor, with a precision of $\pm$0.1 K.

C. NMR simulations

All NMR simulations were performed using home-built programs which use the software package Gamma, version 4.0.5B.[77]

4. H_2@aza-thia-open-cage-fullerene (compound I)

The complex of H_2 with aza-thia-open-cage-fullerene (ATOCF) was the first endohedral H_2-fullerene complex to be synthesized in high yield.[8] The fullerene cage in ATOCF contains an orifice bounded by a 13-membered ring, through which molecular hydrogen is forced at high temperature and pressure.[8] In the following discussion, H_2@ATOCF is referred to as compound **I**. Its molecular structure is shown in Fig. 1.

A. High-temperature spectra

Magic-angle-spinning proton NMR spectra of **I** are shown in Fig. 4a–c. The spinning frequencies used are (a) 2.00 kHz, (b) 6.00 kHz and (c) 10.00 kHz. These spectra were obtained using the simple one-pulse experiment of Fig. 2a.

The strong narrow peak at −7.4 ppm is attributed to the highly mobile endohedral *ortho*-H_2 molecules. The isotropic chemical shift is similar to the reported solution NMR shift of −7.25 ppm.[8] The broader features in the ^{1}H NMR spectra are attributed to the exohedral protons of **I**, with some contributions from the NMR probe components. The endohedral peak becomes narrower as the spinning frequency increases, attaining a width at half-height of only 0.5 ppm at a spinning frequency of 10.00 kHz. The narrowing of the peak with increased spinning frequency may be attributed to the motional averaging of dipole–dipole couplings between the endohedral and exohedral protons by the magic-angle spinning.

The endohedral peak splits into many spinning sidebands at low spinning frequencies. This is due to the anisotropic rotation of the H_2 molecules inside the distorted fullerene cage, which has insufficient symmetry to average out the homonuclear dipole–dipole coupling between the H_2 protons. The order parameter S^2_{HH}, defined in eqn (2.2), is a few percent at room temperature. The motionally-averaged dipole–dipole coupling is modulated by the magic-angle spinning, leading to the prominent spinning sideband patterns in Fig. 4a–c.

B. ^{1}H–^{1}H dipolar recoupling

The existence of a finite ^{1}H–^{1}H dipolar coupling permits the excitation of DQ coherence using a homonuclear recoupling sequence. The spectrum in Fig. 4d shows a DQ-filtered ^{1}H NMR spectrum of **I**, obtained at a spinning frequency of 10.00 kHz using a recoupling sequence (Fig. 2d) with the symmetry $R14^6_2$. The DQ filtering suppresses the exohedral signals, since these participate in a complex multiple-spin coupling network, for which the DQ recoupling experiment is less effective.

The motionally-averaged ^{1}H–^{1}H dipolar coupling may be estimated quantitatively by varying one of the intervals in the DQ pulse sequence (Fig. 2d). The DQ-filtered signal amplitude oscillates as a function of the variable interval, as shown in Fig. 5 for two different temperatures. The motionally-averaged dipole–dipole coupling becomes larger as the temperature is decreased, reflecting an increase in the motional anisotropy of the endohedral H_2 molecules at low temperature. The experimental values of the motionally-averaged dipole–dipole coupling for compound **I** at different temperatures, as determined by DQ recoupling experiments, are shown in Fig. 6 (filled squares).

C. Low-temperature ^{1}H spectra

At sufficiently low temperature, the endohedral H_2 molecules occupy a small number of discrete quantum states, which leads to major changes in the NMR spectra. This phenomenon has

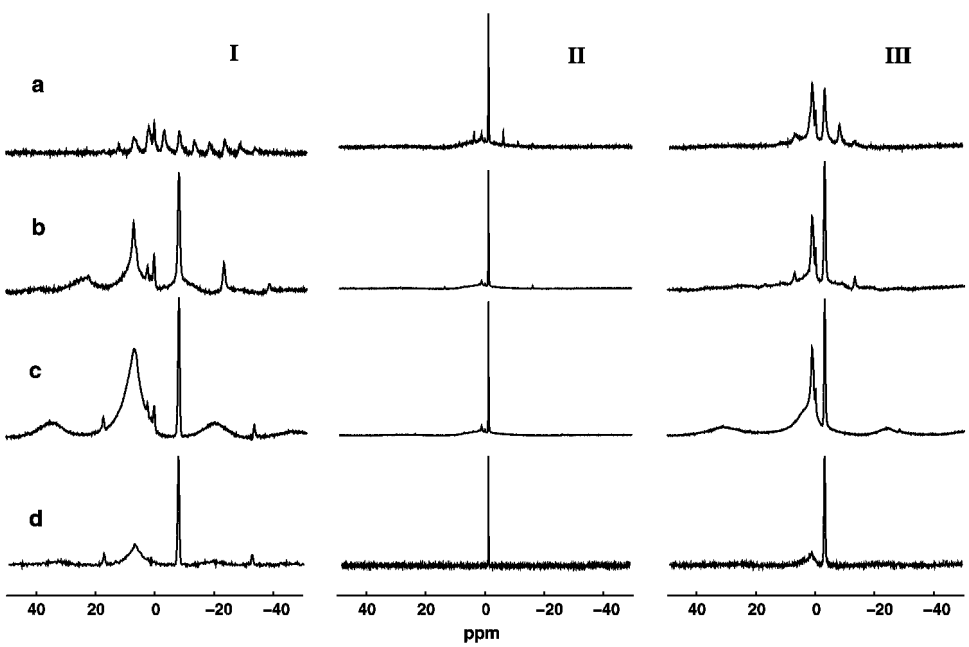

Fig. 4 ^{1}H MAS-NMR spectra of compounds **I–III** at a field of 9.4 T and temperature of 293 K, after baseline correction. The magic-angle spinning frequencies are (a) 2.0 kHz, (b) 6.0 kHz, (c) 10.0 kHz. Row (d) shows double-quantum filtered NMR spectra at a spinning frequency of 10.0 kHz. The recoupling sequences, recoupling durations and DQ-filtering efficiencies were, respectively: (**I**) $R14^6_2$, τ_{exc} = 200.0 μs and 53%. (**II**) SR26, τ_{exc} = 3.4 ms and 30%. (**III**) $R14^6_2$, τ_{exc} = 400 μs and 45%. The data for compound **I** are reused with permission from ref. 28. Copyright (2004) American Chemical Society.

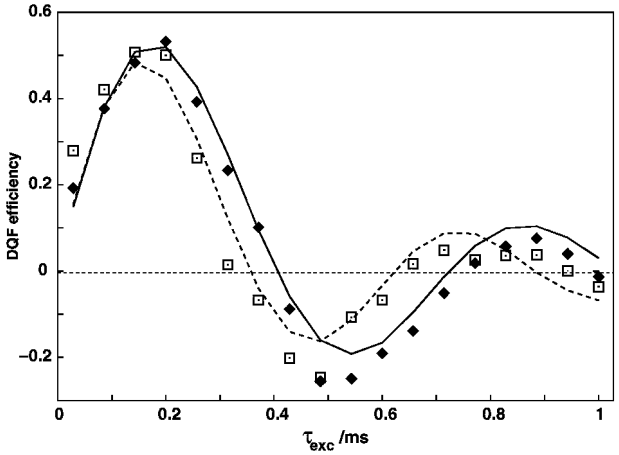

Fig. 5 DQ-filtered signal amplitudes for compound **I** as a function of DQ excitation time τ_{exc}, with the DQ reconversion time τ_{rec} fixed at 200 μs. The magnetic field was 9.4 T and spinning frequency 10.0 kHz. A recoupling sequence with symmetry $R14_2^6$ was used for the DQ recoupling. Diamonds: experimental points at a temperature of 293 K; squares: experimental points at 160 K. Solid line: best fit modulation curve for a dipole–dipole coupling of 6.1 kHz. Dashed line: best fit modulation curve for a dipole–dipole coupling of 7.3 kHz. Reprinted with permission from ref. 28. Copyright (2004) American Chemical Society.

been analyzed in detail in ref. 29. Some static ^{1}H lineshapes are shown as a function of temperature in Fig. 7, column **I**. These spectra were obtained using the Solomon echo sequence, in Fig. 2b, in order to suppress the exohedral proton signals. These data have been interpreted quantitatively in terms of a temperature-dependent biaxial dipole–dipole coupling tensor. A model of quantized rotational and translational states, populated according to the Boltzmann distribution, was used to interpret the dipole–dipole coupling parameters.[29]

Magic-angle-spinning ^{1}H NMR spectra of **I**, obtained at cryogenic temperatures, are shown in the first column of Fig. 8. These spectra were obtained using a MAS frequency of 15.0 kHz and the one-pulse sequence (Fig. 2a). The broad exohedral signals are rather insensitive to the temperature, while the narrow spinning sidebands from the endohedral protons become increasingly numerous as the temperature is decreased, which reflects the increase in the motionally-averaged dipole–dipole interaction. As discussed in ref. 29, the cryogenic MAS data are fully compatible with the static lineshapes, indicating that the rapid sample rotation does not lead to a significant change in sample temperature.

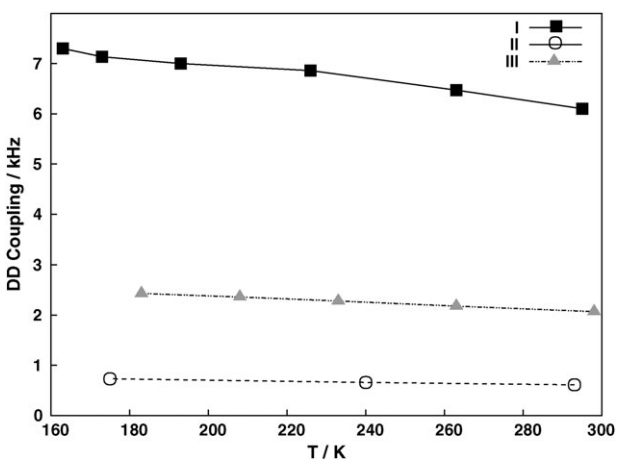

Fig. 6 Temperature dependence of the motionally-averaged ^{1}H–^{1}H dipole–dipole couplings at 10.0 kHz spinning frequency, for compounds **I** and **III** at 9.4 T, and for **II** at 7.0 T. All measurements were performed using the pulse sequence in Fig. 2d. Details on the DQ recoupling schemes for samples **I–III** are given, respectively, in the captions of Fig. 5, Fig. 13 and Fig. 19.

D. ^{1}H spin–lattice relaxation

The room-temperature ^{1}H longitudinal relaxation time constant, T_1, was measured using the inversion-recovery sequence (Fig. 2c). The ^{1}H T_1 values for the exohedral and endohedral protons of compound **I** are shown as function of the rotation frequency in Fig. 9. These time constants were estimated from the dependence of the centre-band peak amplitudes on the relaxation interval. The recovery curves for the longitudinal magnetization components were consistent with a single-exponential dependence on time. At a low spinning frequency, the magnetization reservoirs of the endohedral and exohedral protons are strongly coupled through spin diffusion, which results in one common relaxation time constant. When the spinning frequency is increased beyond a threshold value of around 10 kHz, the spin diffusion is quenched, leading to distinct relaxation time constants for the endohedral and exohedral protons. At high spinning frequency, the relaxation time constants for the exohedral and endohedral protons differ by more than an order of magnitude. Similar phenomena have been observed in other samples.[78] The data in Fig. 9 prove that the rapidly-rotating endohedral H_2 molecules act as relaxation sinks for protons outside the fullerene cage, providing that the MAS frequency is below the spin-diffusion threshold.

The temperature dependence of T_1, observed under static conditions in a field of 8.5 T, is shown for the full range of temperatures in Fig. 10 (filled squares). The spin–lattice relaxation time constant of **I** passes through a broad minimum at a temperature of around 70 K. The value of T_1 at this temperature is 220 ms. As discussed above, the T_1 observed under static conditions is a weighted average of the spin–lattice relaxation time constants of the endohedral and exohedral protons, which equilibrate with each other through spin diffusion. If we assume rapid thermal equilibration between the endohedral and exohedral protons, and assume that the intrinsic T_1 of the exohedral protons is very long at 70 K, then the intrinsic T_1 of the endohedral protons may be estimated to be around 27 ms at 70 K.

Data showing the combined effects of magnetic field, spinning frequency, and temperature on the ^{1}H T_1 of compound **I** are shown in Fig. 11. In the case of the magic-angle-spinning data, the values of T_1 refer to the endohedral H_2 peak alone, and are much smaller than the values obtained under static conditions. This reflects the attenuation of spin diffusion by the magic-angle spinning, as described above.

Fig. 11 shows a strong field-dependence for the endohedral T_1, with the relaxation rate constant decreasing rapidly as the applied magnetic field is increased. This indicates that the

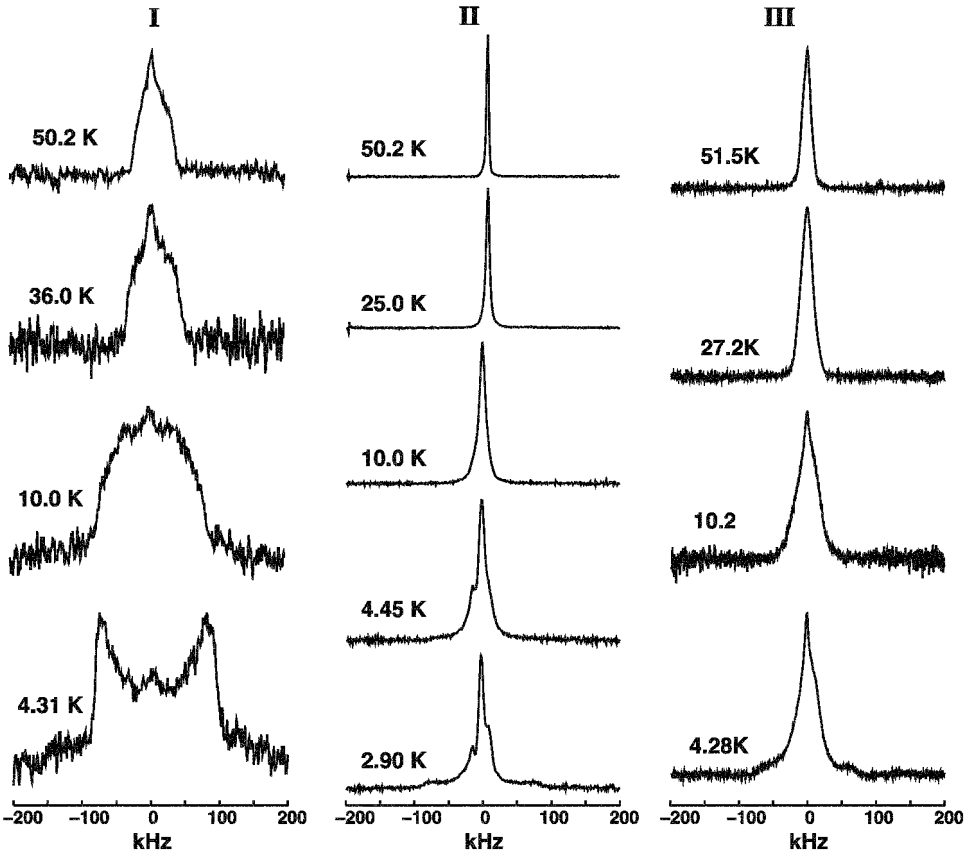

Fig. 7 Experimental ^{1}H spectra of static samples **I**–**III** as a function of temperature in a field of 8.5 T, using a Solomon echo sequence (Fig. 2b) with: (**I**) $\tau = 400$ μs. (**II**) $\tau = 100$ μs. (**III**) $\tau = 200$ μs. The data for compound **I** are reused with permission from ref. 29. Copyright 2006, American Institute of Physics.

correlation time for motionally-induced fluctuations in the dipole–dipole coupling is rather long (order of nanoseconds at room temperature).

E. ^{13}C NMR

The ^{13}C NMR spectrum of **I** is shown in Fig. 12. This was obtained using the RAMP-CP pulse sequence (Fig. 3c) at room temperature. The spectrum contains numerous signals from the exohedral groups and from the cage carbons, which are non-equivalent due to the presence of the low-symmetry orifice. The solid-state ^{13}C spectrum resembles that observed in solution.[10]

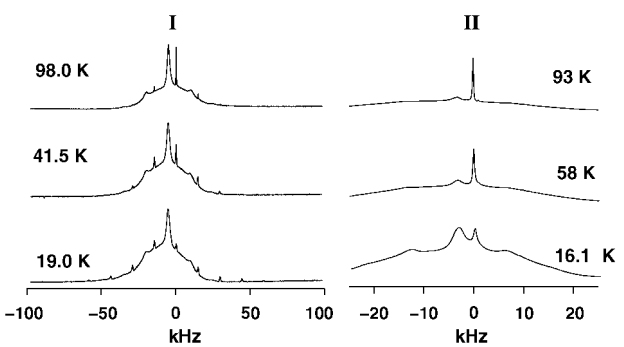

Fig. 8 Experimental ^{1}H MAS spectra of samples **I** and **II** as a function of temperature in a field of 8.5 T. The spinning frequency is 15.0 kHz for **I** and 10.0 kHz for **II**.

5. $H_2@C_{60}$ (compound II)

The symmetrical complex $H_2@C_{60}$ (compound **II** in Fig. 1) was synthesized from H_2@ATOCF (compound **I**) by closing the cage and removing the exohedral groups in a series of organic reactions (9). The $H_2@C_{60}$ molecules were separated

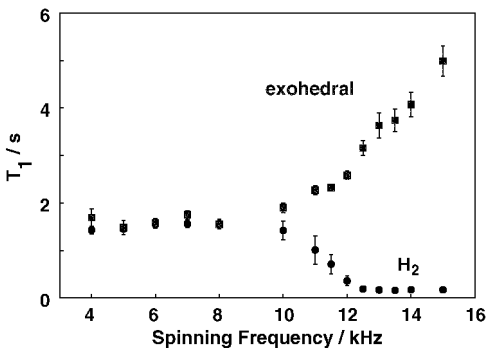

Fig. 9 ^{1}H spin–lattice relaxation time constant T_1 *versus* spinning frequency for compound **I**, at 293 K in a field of 9.4 T. The T_1 values of the endohedral and exohedral protons diverge at high spinning frequency. Reprinted with permission from ref. 28. Copyright (2004) American Chemical Society.

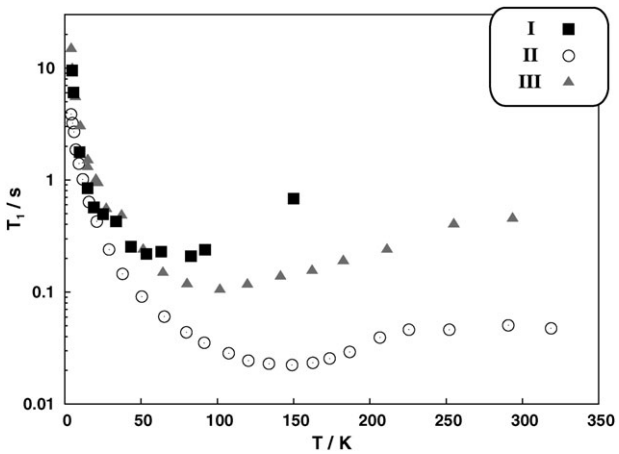

Fig. 10 Experimental ^{1}H spin–lattice relaxation time constants T_1 as a function of temperature for compounds **I**–**III** recorded at 8.5 T on static samples with the inversion recovery sequence.

from the empty C_{60} cages by high-performance HPLC.[9] A high level of purity could therefore be achieved, despite the very small mass difference between C_{60} and $H_2@C_{60}$.

Unlike the other compounds described in this article, **II** displays significant rotational dynamics for the fullerene cages themselves, as well as for the endohedral molecules. As discussed below, this compound has two different phases, which involve different degrees of rotational freedom for the fullerene icosahedra. If magic-angle spinning is performed on **II**, the system under study is a rotor (the sample container), which itself contains rotors (the C_{60} cages), which contain yet more rotors (the H_2 molecules)!

A. High-temperature spectra

Magic-angle-spinning ^{1}H NMR spectra of **II** are shown in the second column of Fig. 4. These spectra were obtained using the one-pulse sequence in Fig. 2a. The isotropic chemical shift of the endohedral H_2 peak is -1.1 ppm, in agreement with the solution NMR.[9] The spinning sidebands of the H_2 peak are barely visible at spinning frequencies above 6 kHz. The absence of spinning sidebands indicates a nearly-isotropic

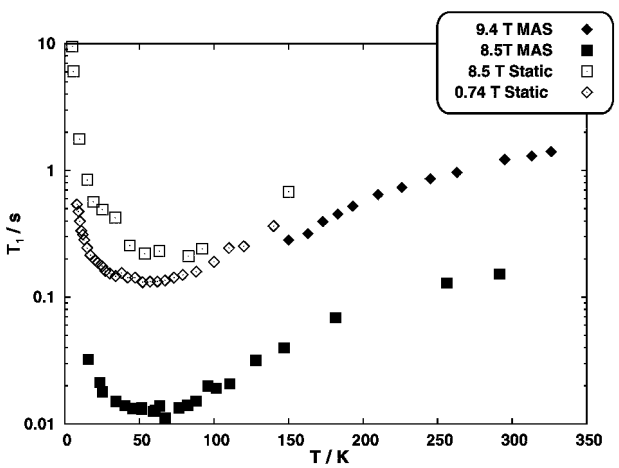

Fig. 11 ^{1}H spin–lattice relaxation time constant T_1 of compound **I**, at various magnetic fields and magic-angle-spinning conditions.

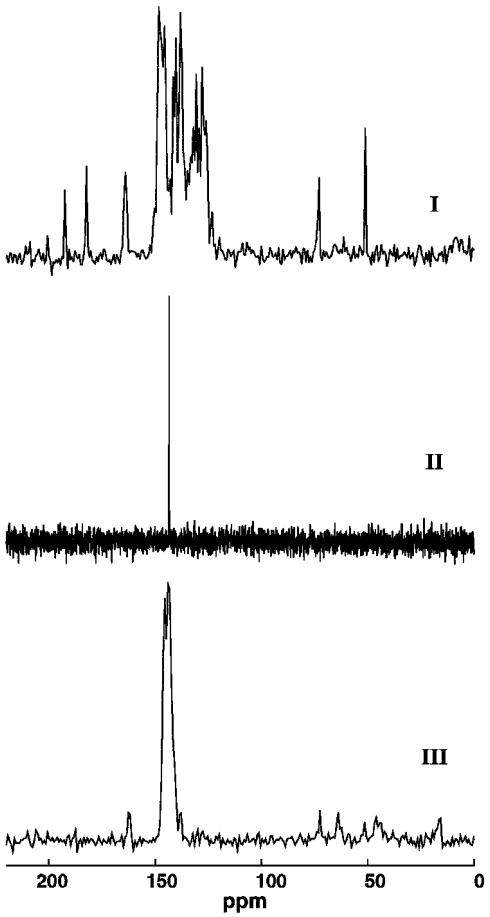

Fig. 12 ^{13}C NMR spectra of samples **I**–**III** recorded in a field of 9.4 T and a temperature of 293 K using cross-polarization from the protons. The experimental conditions were as follows: (**I**) 14.0 kHz MAS, 9 ms contact time and 90.0 kHz SPINAL-64 decoupling. (**II**) 13.0 kHz MAS, 20 ms contact time and no proton decoupling. (**III**) 13.0 kHz MAS, 8 ms contact time and 90.0 kHz SPINAL-64 decoupling.

rotational motion of the molecular hydrogen molecules within the C_{60} cages. The linewidth of the H_2 resonance is only 0.1 ppm at a spinning frequency of 10.0 kHz.

In addition to the narrow endohedral peak, the ^{1}H spectra of **II** display some broad features which are mainly due to the background ^{1}H signal of the probe components. However, there may also be some contributions from impurities and occluded solvent. Different sample preparations display broad components with different intensities. The spectra shown are from the ''cleanest'' preparation we have obtained so far.

B. ^{1}H–^{1}H dipolar recoupling

The second column of Fig. 4d shows a DQ-filtered ^{1}H NMR spectrum of **II**, obtained using the sequence in Fig. 2d, at a spinning frequency of 10.0 kHz. The recoupling technique was SR26, which has a robust performance for relatively weak couplings.[57–60] The DQ-filtered signal is fairly strong, with an amplitude of 30% of the directly-excited signal.

At first sight, the existence of a strong DQ-filtered signal is puzzling, since the intramolecular dipole–dipole coupling between the H_2 protons should be averaged to zero by the

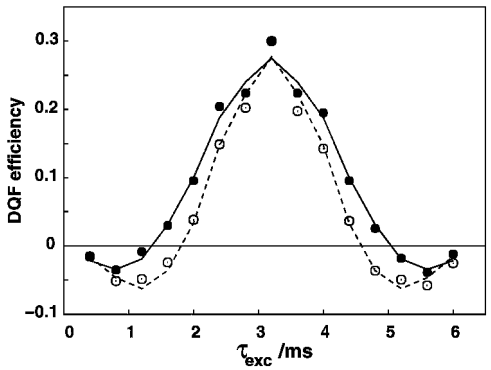

Fig. 13 DQ-filtered signal amplitudes for compound **II** as a function of DQ excitation time τ_{exc}, in a constant time experiment using pulse sequence Fig. 2d and SR26 recoupling,[57–60] with $\tau_{exc} + \tau_{rec} = 6.4$ ms. The magnetic field was 7.0 T and the spinning frequency was 10.0 kHz. Solid circles and solid line: experimental points and best fit at 293 K to an isolated spin-pair simulation with a dipole–dipole coupling of −610 Hz. Open circles and dashed line: experimental points and best fit at 175 K to an isolated spin-pair simulation with a dipole–dipole coupling of −730 Hz.

rotation inside the icosahedral cage, assuming that the solid-state environment preserves the symmetry.

The nature of the DQ-filtered signal was explored further by performing dipolar recoupling experiments as a function of excitation interval τ_{exc} at a series of temperatures, using the constant time approach.[57,61,62] The SR26 sequence was used in all cases. Some of the experimental data sets are shown in Fig. 13. The curves were fitted to numerical simulations for isolated two-spin systems, by varying the dipole–dipole coupling constant. The corresponding best fits for a few temperature points are shown in Fig. 13. The temperature dependence of the best fit dipole–dipole couplings is weak, as shown in Fig. 6. These data should be regarded as qualitative, since an isolated two-spin model is known to be unrealistic for this case (see below).

The ^{1}H–^{1}H dipolar interaction observed in **II** is smaller than that observed in **I** by one order of magnitude. However, even this small residual coupling is unexpected for dihydrogen trapped in an icosahedral cage. The nature of the DQ-filtered signal was explored further by spherical tensor analysis (STA) of the nuclear spin density operator,[63] using the pulse sequence in Fig. 2e. The results of experiments performed at a spinning frequency of 10.0 kHz are shown in Fig. 14. At a short recoupling time of 0.4 ms (Fig. 14a), only density operator components with rank 1 are significant, corresponding to thermal Zeeman polarization. When the recoupling interval increases to 0.8 ms (Fig. 14b), tensor components with rank 2 and quantum orders ±2 appear, indicating the action of DQ recoupling. The appearance of a rank 3 component after only 1.6 ms of recoupling (Fig. 14c) is a clear signature of significant intermolecular interactions. The situation is unambiguous after 3.2 ms, where tensor components up to rank 5 are clearly present. This proves that at least part, if not all, of the DQ-filtered signal in Fig. 4d originates from intermolecular spin–spin interactions between endohedral hydrogen molecules in neighbouring cages. Further work is in progress on this issue.

C. Low-temperature spectra

Static ^{1}H NMR spectra of **II** were obtained with the Solomon echo (Fig. 2b) at a set of different temperatures in the cryogenic regime. The results are shown in the second column of Fig. 7. The lineshapes are remarkably narrow down to the lowest accessible temperatures. Asymmetric spectral features appear at temperatures below around 5 K. These features may simply be artefacts associated with magnetic distortions in the probe at cryogenic temperatures. However, it is also possible that these lineshapes reflect genuine quantum dynamics in the freely-rotating H_2 molecules, and could be related to the spin-rotation and rotational magnetic resonance phenomena which are observed in molecular beams.[79–81] This is an intriguing possibility which is currently under investigation.

Cryogenic MAS experiments were performed at a spinning frequency of 10.0 ± 0.3 kHz using a simple one-pulse procedure (Fig. 2a). The ^{1}H spectra are shown in the second column of Fig. 8. The spinning sideband pattern is absent in this case, reflecting the much smaller size of the anisotropic couplings for **II**, even at the lowest accessible temperatures. The low-temperature spectra have poor quality, with relatively large broad signals from impurities and/or probe background signals. The poor signal strength for the endohedral ^{1}H signals at the lowest temperatures is not currently understood.

D. ^{1}H spin–lattice relaxation

The spin–lattice relaxation time constant T_1 of **II** was determined as a function of magnetic field and temperature. The results are presented in Fig. 15, which also includes published solution-state T_1 data for **II** dissolved in toluene-d_8.[12]

For solid samples, the ^{1}H T_1 of **II** passes through a minimum as a function of temperature, before reaching a region which is almost independent of both field and temperature above 200 K. The temperature and the depth of the T_1-minimum below 200 K are strongly field-dependent.

The observation that the T_1 minimum shifts to *higher* temperature on going from **I** to **II** is surprising. We are currently exploring theoretical models of spin–lattice relaxation for the endohedral H_2 molecules, which take into account the influence of cage symmetry on the coupling between the translational and rotational motion of the endohedral species.

The ^{1}HT_1 values for the solid samples are unlike the solution data, in which the T_1 exhibits a weak *maximum* around 250 K.[12] The discrepancy between the solid and solution values of T_1 indicates that the thermal motion of the C_{60} *cages* must contribute to the endohedral H_2 relaxation in solutions of **II**.

E. ^{13}C NMR

The ^{13}C NMR of **II** is of great interest, since even pure C_{60} displays a rich range of phenomena associated with motional phase transitions.[36] Above 170 K, the C_{60} icosahedra rotate rapidly and isotropically, leading to a single narrow ^{13}C NMR peak even in the absence of magic-angle spinning.[33] Below this temperature, the ^{13}C NMR spectrum of C_{60} displays two components: a sharp, mobile component, and a broader shape associated with the immobilized fullerene cages, which display considerable chemical shift anisotropy. Complete freezing of

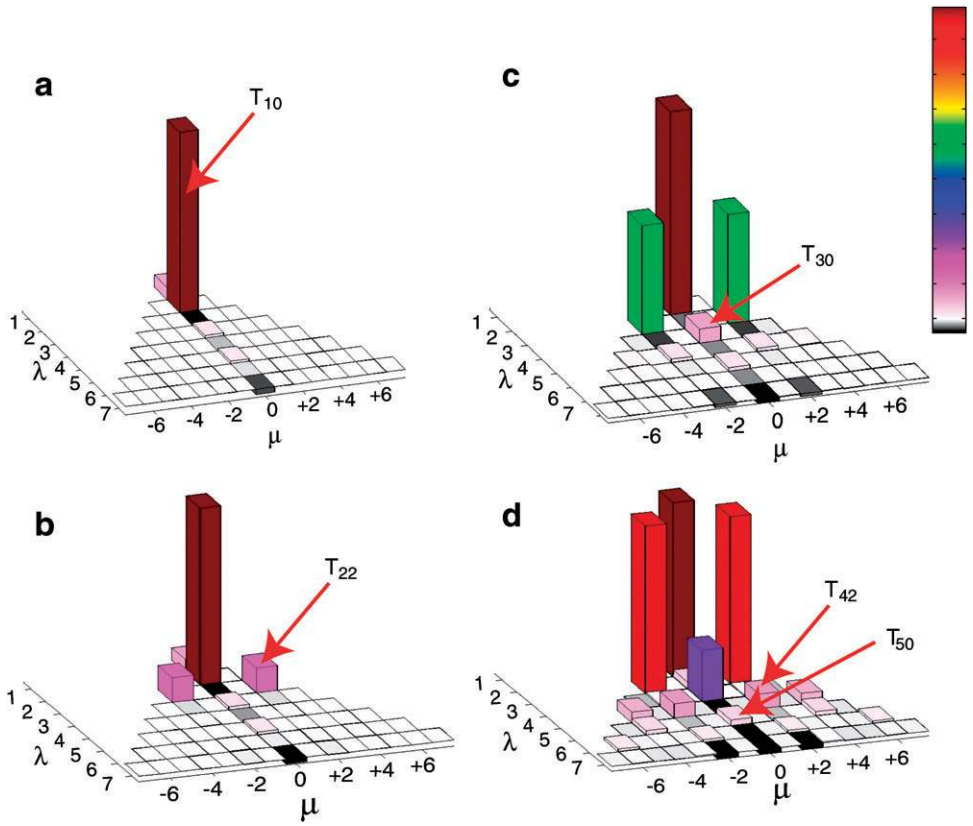

Fig. 14 Spherical tensor analysis of a ^{1}H DQ recoupling experiment performed on sample **II** in a field of 7.0 T at a spinning frequency of 10.0 kHz, using the sequence in Fig. 2e and SR26 double-quantum recoupling.[57–60] Identical recoupling intervals τ_{exc} and τ_{rec} were used, with values as follows: (a) 0.4 ms, (b) 0.8 ms, (c) 1.6 ms, (d) 3.2 ms. The amplitudes of spherical tensor components with rank λ and quantum order μ are indicated by the height of the corresponding box as well as the colour code. The emergence of components with rank greater than 2 indicates the participation of intermolecular spin–spin interactions.

the cage rotation is achieved at temperatures below around 140 K.[33]

The room-temperature magic-angle-spinning ^{13}C NMR spectrum of **II**, obtained by cross-polarization from the protons (Fig. 3c) is shown in the second column of Fig. 12. The spectrum displays a single very narrow ^{13}C line (7 Hz wide) at 143.0 ppm relative to TMS,[82] and was recorded without any ^{1}H decoupling and without a ramp in the ^{13}C field, since the Hartmann–Hahn matching condition is very narrow for this compound. The transfer of polarization from the protons to ^{13}C is very slow and we observe a smooth increase in the CP signal strength up to a contact time of 20 ms. So far, we did not resolve any structure in the ^{13}C peak, which would be anticipated if empty fullerene cages were present (0.078 ppm downshift from solution data[9]), or if the ^{13}C chemical shift was sensitive to the distinction between *ortho*- and *para*-hydrogen guest molecules.

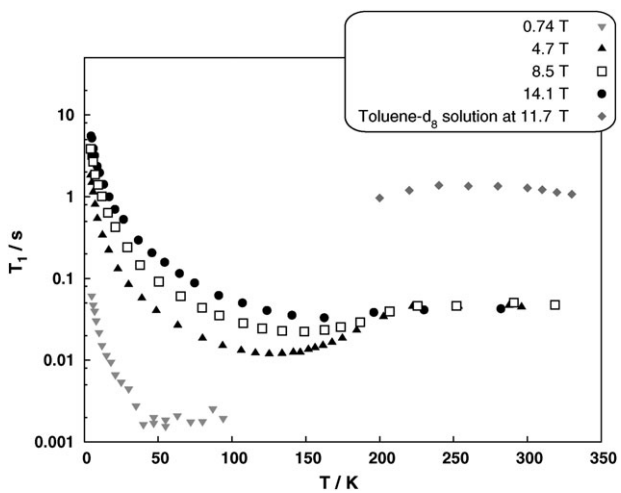

Fig. 15 Experimental ^{1}H T_1 *versus* temperature for static samples of **II** measured at several magnetic fields. The ^{1}H T_1 values for a solution of **II** in toluene-d_8 are also shown. The toluene-d_8 solution data are adapted from ref. 12.

Fig. 16 shows the results of experiments performed on static samples of **II** using the Carr–Purcell echo sequence of Fig. 3b. These spectra were recorded without cross-polarization from the protons and without proton decoupling. The behaviour of the ^{13}C spectrum as a function of temperature is very similar to that observed for pure C_{60}, with a broad spectral component appearing below $\sim$130 K and dominating the spectrum below $\sim$100 K. These temperatures are about 10–20 K lower than those observed for pure C_{60}.[33] The low-temperature lineshape corresponds to a single site with chemical shift anisotropy parameters of $\{\delta^{aniso}, \eta\} = \{-109.5 \pm 5$ ppm, $0.20 \pm 0.15\}$ (using the deshielding convention for chemical shifts). These parameters are consistent with those observed for pure C_{60}

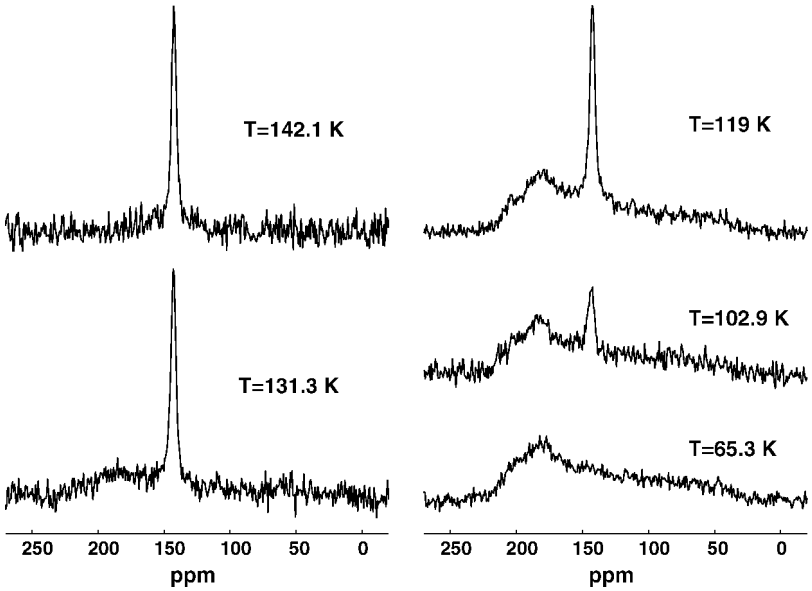

Fig. 16 Experimental ^{13}C spectra of a static sample of **II** in a field of 14.1 T as a function of temperature. All spectra were obtained using a Carr–Purcell echo, with $\tau = 80$ μs and no ^{1}H decoupling.

($\{\delta^{aniso}, \eta\} = \{-109.6, 0.28\}$, see ref. 33), indicating that the perturbation of the ^{13}C chemical shift principal values by the H_2 guest is too small to be detected.

Fig. 17 shows magic-angle-spinning ^{13}C spectra at four different temperatures. These were obtained using cross-polarization of the ^{13}C magnetization from the endohedral protons. The ^{13}C signals were acquired without ^{1}H decoupling. These spectra were difficult to obtain in the cryogenic regime, since the Hartmann–Hahn matching condition is very sharp, and the spinning frequency relatively unstable. Fig. 17 shows spectral features that are qualitatively similar to those in Fig. 16. Spinning sidebands appear at temperatures below $\sim$130 K due to the chemical shift anisotropy of the immobilized fullerene cages.

Measurements of the ^{13}C spin–lattice relaxation time constant in **II** were performed with the saturation-recovery pulse sequence (Fig. 3d) at 14.1 T and without proton decoupling. The results are shown in Fig. 18. They display a gradual decrease of T_1 with increasing temperature below around 230 K, followed by a steep increase of T_1 with temperature in the region between 230 and 240 K, beyond which T_1 increases roughly linearly with respect to temperature. This behaviour is qualitatively similar to that observed in pure C_{60}.[33]

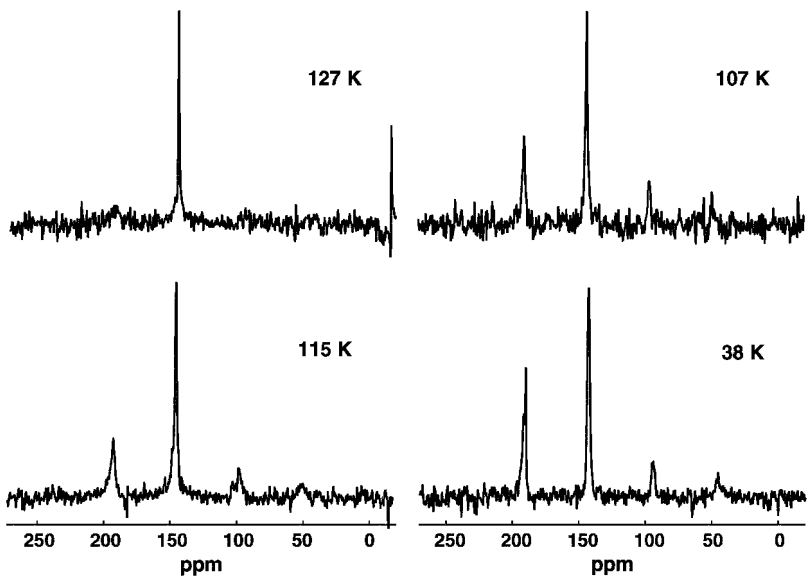

Fig. 17 Experimental ^{13}C spectra of **II** in a field of 8.5 T as a function of temperature with a MAS rotation frequency of 4.2 ± 0.3 kHz. All spectra were obtained using cross-polarization from the protons, with a contact time of 3 ms and no ^{1}H decoupling during signal acquisition.

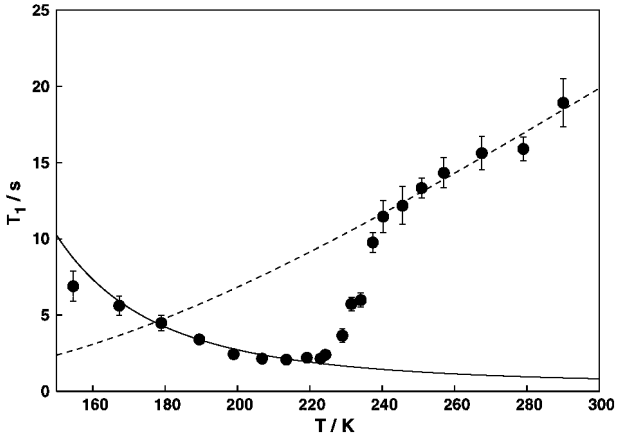

Fig. 18 Symbols: experimental values of ^{13}C T_1 as a function of temperature, on a static sample of **II** in a field of 14.1 T. The T_1 values from eqn (5.3) are shown below the transition temperature (solid line) and above the transition temperature (broken line), using the best-fit parameters given in Table 1.

The sharp increase in the ^{13}C T_1 between 230 and 240 K may be attributed to a phase transition, in which the rotational motion of the C_{60} changes from a low-temperature phase, in which the molecules reorient in large-angle jumps, to a high-temperature phase, in which the cages undergo rapid rotational diffusion.[33,36] However, the sharp increase in T_1 occurs in pure C_{60} at around 260 K, *i.e.* 30° higher than in **II**. It would be of interest to explore the thermodynamics of the phase transition in **II** by differential scanning calorimetry. However, no such studies have yet been performed.

The ^{13}C relaxation in the temperature range above around 180 K may be described by a model in which the CSA tensor is modulated by thermally-activated rotational diffusion of the fullerene cages. An expression for the relaxation rate constant in this model has been given by Abragam:[83]

$$T_1^{-1} = \frac{3}{20}\omega_0(\delta^{\mathrm{aniso}})^2(1+\eta^2/3)\frac{2\omega_0\tau_c}{1+(\omega_0\tau_c)^2} \qquad (5.3)$$

where ω_0 is the Larmor frequency, δ^{aniso} is the magnitude of the CSA, η is the biaxiality of the CSA tensor, and τ_c is the rotational correlation time. The temperature dependence of T_1 may be treated by assuming that the correlation time τ_c follows the Arrhenius law

$$\tau_c^{-1} = (\tau_c^0)^{-1}\exp\{-E_a/k_BT\} \qquad (5.4)$$

where E_a is the activation energy for the motional process. Since the CSA is known from the static NMR spectra at low temperature, the parameters τ_c^0 and E_a may be determined by fitting the experimental T_1 data. Different sets of parameters are required for the two phases, below and above the transition temperature at around 235 K.

The best-fit rotational parameters are summarized in Table 1. The predicted temperature dependence of T_1 in the two phases is shown by the lines in Fig. 18. For the sake of comparison, Table 1 also shows the parameters for pure C_{60}, as determined by fitting the data reported in ref. 33, using the same model >eqn (5.3) and eqn (5.4)].

The activation energy for the rotational jump motion in the low-temperature phase is found to be considerably lower for **II** compared to that for pure C_{60}. This indicates that the endohedral H_2 molecules have an appreciable effect on the non-bonding interactions between neighbouring C_{60} cages. The non-bonding interactions appear to have a weaker directionality in **II** compared to C_{60}, offering a lower hindering potential to rotational jumps. The shift of the rotational transition to lower temperatures for **II** compared to pure C_{60} agrees with the lineshape data, where the appearance of the broad CSA powder pattern occurs at lower temperatures for **II** compared to C_{60}.[33]

6. H_2@di(ethoxycarbonyl)methanofullerene (compound III)

Compound **III** in Fig. 1 was synthesized from **II** by the procedure described in ref. 10. Our main motivation for studying **III** was to investigate how a relatively small distortion of the cage geometry influences the ^1H relaxation. At present, compound **III** is only available in small quantities (a few milligrams), which places some restrictions on the NMR experiments that may be performed.

A. High-temperature spectra

Magic-angle-spinning ^1H NMR spectra of **III** are shown in the third column of Fig. 4. The spectra display a strong narrow peak from the endohedral H_2 molecules at −3.0 ppm as well as broader features from the exohedral ethyl groups.

B. ^1H–^1H dipolar recoupling

Dipolar recoupling experiments were performed using sequence Fig. 2d with $R14_2^6$. A double-quantum filtered ^1H spectrum of **III** obtained using recoupling sequences with the symmetry is shown in the third column of Fig. 4d. Once again the endohedral proton signals pass readily through the double-quantum filter, while the exohedral proton signals are partially suppressed.

Fig. 19 shows the dependence on the double-quantum-filtered signal amplitude on the recoupling pulse sequence durations, varied according to the constant time protocol.

Table 1 Parameters for the temperature-dependence of the ^{13}C T_1 in compound **II** and in pure C_{60}. Separate parameters are reported for the temperature ranges above and below the rotational phase transition. CSA parameters of $\delta^{\mathrm{aniso}} = -109$ ppm and $\eta = 0.2$ were assumed. The C_{60} data were adapted from ref. 33

Sample	H_2@C_{60}		C_{60}	
Fit range	$170 \le T \le 224$ K	$240 \le T \le 300$ K	$193 \le T \le 243$ K	$263 \le T \le 323$ K
E_a/kJ mol^{-1}	6.7	5.3	20.6	4.4
τ_c^0/ps	178.6	1.8	0.23	2.1

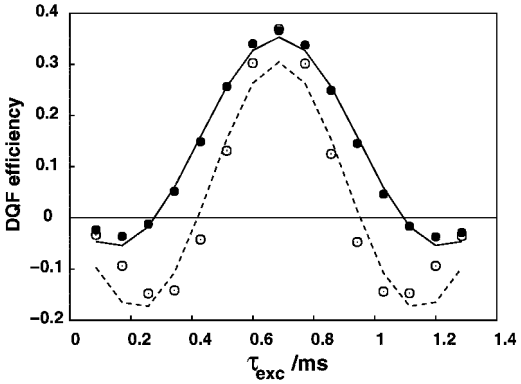

Fig. 19 DQ-filtered signal amplitudes for compound **III** as a function of DQ excitation time τ_{exc}, in a constant time experiment with $\tau_{exc} + \tau_{rec} = 1.37$ ms using the pulse sequence in Fig. 2d and a recoupling sequence with the symmetry $R14_6^6$. The magnetic field was 9.4 T and the spinning frequency 10.0 kHz. Solid circles: experimental signal amplitudes at 293 K. Solid line: best fit to an isolated spin-pair simulation with a dipole–dipole coupling of −2.07 kHz. Open circles: experimental signal amplitudes at 185 K. Broken line: best fit to an isolated spin-pair simulation with a dipole–dipole coupling of −2.43 kHz.

The experimental results are displayed for two different temperatures, together with the corresponding best-fit simulations. The data analysis was performed using home-built programs assuming a two-spin model. Deviations in the fits may be attributed to multi-spin effects while lead to couplings between endohedral and exohedral protons.

As in the case of compounds **I** and **II**, we observe a moderate temperature dependence of the effective dipole–dipole coupling constant, which increases in magnitude as the sample is cooled. The temperature dependence of the dipole–dipole coupling constant is plotted in Fig. 6. As expected, the magnitudes of the dipole–dipole coupling constants are in the order **II** < **III** < **I**. This conforms to physical expectations, since the dipole–dipole coupling constant is proportional to the rotational anisotropy of the molecular hydrogen molecules, which is determined by the geometry of the cage. Compound **II** has an undistorted fullerene cage, while compound **I** has a grossly distorted cage containing an orifice.

C. Low-temperature ^{1}H spectra

Static ^{1}H NMR spectra of **III** were obtained using the Solomon echo sequence (Fig. 2b) at a set of different temperatures in the cryogenic regime. The results are shown in the third column of Fig. 7. There is a moderate temperature dependence in the line shape, with significant broadening appearing below ~10 K and some distinct spectral features appearing at around 4 K. At the current time, it is not clear whether this behaviour reflects genuine spin dynamics or is simply an instrumental artefact.

MAS NMR spectra of **III** have not yet been obtained in the cryogenic temperature regime.

D. ^{1}H spin–lattice relaxation

The ^{1}H spin–lattice relaxation time constant T_1 of **III** was determined as a function of temperature at a fixed magnetic field of 8.5 T. MAS was not used. The results are shown in Fig. 10.

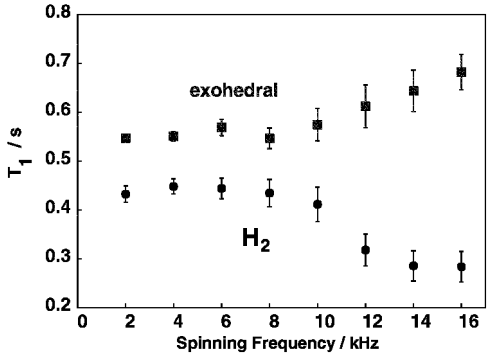

Fig. 20 ^{1}H T_1 *versus* spinning frequency for **III** in a field of 9.4 T.

The T_1 behaviour is intermediate between the low-symmetry complex **I** and the high-symmetry complex **II**. The results on these three compounds suggest a correlation between the symmetry of the cage and the temperature at the T_1 minimum. This is an important result which will guide the synthesis of complexes with T_1 minima at temperatures lower than 50 K. A relaxation theory which is capable of explaining this phenomenon is under development.

The resonances of the exohedral and endohedral protons are partially resolved by magic-angle spinning. It is therefore possible to explore the T_1 of both sets of protons as a function of the MAS frequency. Results obtained at room temperature are shown in Fig. 20. As in the case of **I**, the results are roughly independent of spinning frequency below around 8 kHz, but display a divergence of the T_1 values for the two proton species above 8 kHz. The data reveal the role of spin diffusion in allowing communication between the two proton spin reservoirs at low spinning frequencies, and the disruption of this magnetization exchange pathway at high spinning frequencies. As shown in Fig. 20, complex **III** behaves differently with respect to complex **I**, in that a finite difference in spin–lattice relaxation rates between the two proton species persists even at low spinning frequencies. The protons in the sample do not relax as a homogeneous reservoir, even under static conditions. This may be due to the relatively high mobility of the exohedral protons of **III** at room temperature.

E. ^{13}C NMR

The ^{13}C CP spectrum of **III** is shown in Fig. 12c. This was obtained using the RAMP-CP pulse sequence (Fig. 3) at room temperature. The substitution on the cage breaks the symmetry and hinders the fast fullerene rotation, giving rise to many closely spaced lines near 143 ppm.

7. Discussion

The solid-state NMR behaviour of endohedral dihydrogen–fullerene complexes is very rich and displays a large number of interesting effects, some of which present fascinating theoretical challenges.

^{1}H NMR spectra reveal the influence of the cage symmetry on the isotropy of the H_2 tumbling motion. High-temperature

spectra indicate that the dihydrogen molecules tumble more anisotropically in less symmetrical cages, which is not too surprising. However, the most interesting phenomena emerge at cryogenic temperatures, where the H_2 rotation becomes quantized and interacts strongly with the quantized translation of the molecule inside the cavity. For the very asymmetric cavity of compound **I**, the H_2 freezes into a discrete quantum state with definite rotational orientation at the lowest temperatures. At slightly higher temperatures, the NMR spectrum is consistent with thermal jumps between a small number of discrete rotational quantum states.[29]

The cryogenic proton NMR spectra of the symmetrical compound **II** and the slightly distorted compound **III** display asymmetrical spectral features which are more difficult to explain. As mentioned above, these spectral features may have an instrumental origin but may also indicate a genuine spin dynamical phenomenon involving entanglement of the nuclear spin dynamics and the spatial quantum dynamics. Further work is required to clarify the situation.

Cryogenic magic-angle spinning NMR data are generally consistent with the data obtained on static samples. There is little evidence of sample heating induced by magic-angle spinning in the cryogenic regime.[29] The low viscosity and high thermal conductivity of cold He gas appear to minimize such heating effects.

The most striking feature of the MAS-NMR spectra are the very narrow spectral lines for the endohedral species, even at very low temperatures, and the development of multiple spinning sidebands as the samples are cooled into the cryogenic regime.

The ^{1}H spin–lattice relaxation behaviour is intriguing. The measurements on compounds **I**, **II** and **III** indicate that increasing symmetry of the cavity leads to a shift in the T_1-minimum towards higher temperatures. This behaviour is somewhat counter-intuitive and also demands theoretical understanding. The issue is of practical importance for the application of these complexes as relaxation sinks for NMR experiments at very low temperatures.

For the most part, ^{1}H–^{1}H dipolar recoupling measurements behave as expected. A more distorted cavity leads to a greater residual dipole–dipole coupling between the H_2 protons, when averaged over the rotational tumbling. The dipole–dipole coupling is weakly temperature-dependent, as expected for a thermal tumbling process in an anisotropic potential. The measurement on the symmetrical complex **II** reveals a small but finite dipole–dipole coupling, despite the icosahedral symmetry of the cage. Spherical tensor analysis shows that this behaviour involves dipole–dipole couplings between endohedral protons in neighbouring cages.

The ^{13}C NMR spectra are unsurprising for compounds **I** and **III**, where the cage symmetry is broken and the rotation of the fullerenes is quenched. A forest of ^{13}C peaks is observed, reflecting the inequivalence of the ^{13}C sites in the broken-symmetry cages. The most interesting behaviour is found for the symmetrical compound **II**, which displays rotational dynamics for the fullerene cages, similar to that observed in pure C_{60}. The ^{13}C spectra and relaxation measurements indicate a phase transition in compound **II**. At temperatures lower than the phase transition, ^{13}C relaxation is driven in part by infrequent large-angle rotational jumps of the cages. At temperatures above the transition, the cages rotate rapidly and isotropically, leading to a narrow ^{13}C NMR peak. The phase transition occurs at a temperature that is around 30 K lower than that found in pure C_{60}. In addition, the ^{13}C relaxation data indicate a lower activation energy for the thermally-activated C_{60} rotations in **II** compared to that in C_{60}. Both observations suggest that the endohedral H_2 molecules weaken the intermolecular interactions between the C_{60} cages, or at least reduce their directionality.

Acknowledgements

This research was supported by the Basic Technology program (UK). M.C. would like to thank Jacco van Beek for discussions and for the matNMR freeware,[84] used frequently during this research. I.H., R.S. and A.S. wish to thank the Estonian Science Foundation for financial support.

References

1 D. S. Bethune, R. D. Johnson, J. R. Salem, M. S. Devries and C. S. Yannoni, *Nature*, 1993, **366**, 123–128.
2 M. Saunders, H. A. Jiménez-Vázquez, R. J. Cross, S. Mroczkowski, D. I. Freedberg and F. A. L. Anet, *Nature*, 1994, **367**, 256–258.
3 M. Saunders, R. J. Cross, H. A. Jiménez-Vázquez, R. Shimshi and A. Khong, *Science*, 1996, **271**, 1693–1697.
4 D. E. Giblin, M. L. Gross, M. Saunders, H. A. Jiménez-Vázquez and R. J. Cross, *J. Am. Chem. Soc.*, 1997, **119**, 9883–9890.
5 Y. Rubin, T. Jarrosson, G. W. Wang, M. D. Bartberger, K. N. Houk, G. Schick, M. Saunders and R. J. Cross, *Angew. Chem., Int. Ed.*, 2001, **40**, 1543.
6 C. M. Stanisky, J. Cross, R. J. Cross, M. Saunders, M. Murata, Y. Murata and K. Komatsu, *J. Am. Chem. Soc.*, 2005, **127**, 299–302.
7 Y. Murata, M. Murata and K. Komatsu, *Chem.–Eur. J.*, 2003, **9**, 1600–1609.
8 Y. Murata, M. Murata and K. Komatsu, *J. Am. Chem. Soc.*, 2003, **125**, 7152–7153.
9 K. Komatsu, M. Murata and Y. Murata, *Science*, 2005, **307**, 238–240.
10 M. Murata, Y. Murata and K. Komatsu, *J. Am. Chem. Soc.*, 2006, **128**, 8024–8033.
11 Y. Matsuo, H. Isobe, T. Tanaka, Y. Murata, M. Murata, K. Komatsu and E. Nakamura, *J. Am. Chem. Soc.*, 2005, **127**, 17148–17149.
12 E. Sartori, M. Ruzzi, N. J. Turro, J. D. Decatur, D. C. Doetschman, R. G. Lawler, A. L. Buchachenko, Y. Murata and K. Komatsu, *J. Am. Chem. Soc.*, 2006, **128**, 14752–14753.
13 T. A. Murphy, T. Pawlik, A. Weidinger, M. Hohne, R. Alcala and J. M. Spaeth, *Phys. Rev. Lett.*, 1996, **77**, 1075–1078.
14 A. Weidinger, M. Waiblinger, B. Pietzak and T. A. Murphy, *Appl. Phys. A: Mater. Sci. Process.*, 1998, **66**, 287–292.
15 J. Lu, Y. S. Zhou, X. W. Zhang and X. G. Z. Xg, *Mol. Phys.*, 2001, **99**, 1199–1202.
16 H. Shinohara, *Rep. Prog. Phys.*, 2000, **63**, 843–892.
17 M. Rubsam, P. Schweitzer and K. P. Dinse, *J. Phys. Chem.*, 1996, **100**, 19310–19314.
18 Z. Q. Shi, X. Wu, C. R. Wang, X. Lu and H. Shinohara, *Angew. Chem., Int. Ed.*, 2006, **45**, 2107–2111.
19 M. D. Diener, J. M. Alford, S. J. Kennel and S. Mirzadeh, *J. Am. Chem. Soc.*, 2007, **129**, 5131–5138.
20 S. I. Iwamatsu and S. Murata, *Tetrahedron Lett.*, 2004, **45**, 6391–6394.
21 S. Iwamatsu, S. Murata, Y. Andoh, M. Minoura, K. Kobayashi, N. Mizorogi and S. Nagase, *J. Org. Chem.*, 2005, **70**, 4820–4825.
22 S. Iwamatsu, C. M. Stanisky, R. J. Cross, M. Saunders, N. Mizorogi, S. Nagase and S. Murata, *Angew. Chem., Int. Ed.*, 2006, **45**, 5337–5340.
23 C. R. Bowers and D. P. Weitekamp, *Phys. Rev. Lett.*, 1986, **57**, 2645–2648.

24 J. Natterer and J. Bargon, *Prog. Nucl. Magn. Reson. Spectrosc.*, 1997, **31**, 293–315.
25 S. B. Duckett and C. J. Sleigh, *Prog. Nucl. Magn. Reson. Spectrosc.*, 1999, **34**, 71–92.
26 P. F. Newhouse and K. C. McGill, *J. Chem. Educ.*, 2004, **81**, 424–426.
27 P. M. Rafailov, C. Thomsen, A. Bassil, K. Komatsu and W. Bacsa, *Phys. Status Solidi*, 2005, **242**, R106–R108.
28 M. Carravetta, Y. Murata, M. Murata, I. Heinmaa, R. Stern, A. Tontcheva, A. Samoson, Y. Rubin, K. Komatsu and M. H. Levitt, *J. Am. Chem. Soc.*, 2004, **126**, 4092–4093.
29 M. Carravetta, O. G. Johannessen, M. H. Levitt, I. Heinmaa, R. Stern, A. Samoson, A. J. Horsewill, Y. Murata and K. Komatsu, *J. Chem. Phys.*, 2006, **124**, 104507.
30 M. S. Conradi, K. Luszczynski and R. E. Norberg, *Phys. Rev. B: Condens. Matter*, 1979, **20**, 2594–2616.
31 M. Tomaselli and B. H. Meier, *J. Chem. Phys.*, 2001, **115**, 11017.
32 M. Tomaselli, *Mol. Phys.*, 2003, **101**, 3029–3051.
33 R. Tycko, G. Dabbagh, R. M. Fleming, R. C. Haddon, A. V. Makhija and S. M. Zahurak, *Phys. Rev. Lett.*, 1991, **67**, 1886–1889.
34 R. Tycko and S. O. Smith, *J. Chem. Phys.*, 1993, **98**, 932–943.
35 R. Tycko, *Sol. State Nucl. Magn. Reson.*, 1994, **3**, 303.
36 W. I. F. David, R. M. Ibberson, T. J. S. Dennis, J. P. Hare and K. Prassides, *Europhys. Lett.*, 1992, **18**, 219–225.
37 G. Navon, Y.-Q. Song, T. Rõõm, S. Appelt, R. E. Taylor and A. Pines, *Science*, 1996, **271**, 1848.
38 D. A. Hall, D. C. Maus, G. J. Gerfen, S. J. Inati, L. R. Becerra, F. W. Dahlquist and R. G. Griffin, *Science*, 1997, **276**, 930.
39 J. H. Ardenkjaer-Larsen, B. Fridlund, A. Gram, G. Hansson, L. Hansson, M. H. Lerche, R. Servin, M. Thaning and K. Golman, *Proc. Natl. Acad. Sci. U. S. A.*, 2003, **100**, 10158–10163.
40 J. Haupt, *Z. Naturforsch.*, 1971, **26a**, 1578–1589.
41 J. Haupt, *Phys. Lett. A*, 1972, **38**, 389.
42 A. Hackmann, H. Seidel, R. D. Kendrick, P. C. Myhre and C. S. Yannoni, *J. Magn. Reson.*, 1988, **79**, 148–153.
43 P. C. Myhre, G. G. Webb and C. S. Yannoni, *J. Am. Chem. Soc.*, 1990, **112**, 8991–8992.
44 A. Samoson, T. Tuherm, J. Past, A. Reinhold, T. Anupõld and I. Heinmaa, *Top. Curr. Chem.*, 2004, **246**, 15–31.
45 M. Mehring, *High Resolution NMR in Solids*, Springer, Berlin, 1982.
46 K. Schmidt-Rohr and H. W. Spiess, *Multidimensional Solid-State NMR and Polymers*, Academic Press, London, 1994.
47 M. J. Duer, *Introduction to Solid-State NMR Spectroscopy*, Blackwell Science, Oxford, 2004.
48 M. H. Levitt, *Spin Dynamics. Basics of Nuclear Magnetic Resonance*, Wiley, Chichester, 2001.
49 I. Solomon, *Phys. Rev.*, 1958, **110**, 61.
50 S. Dusold and A. Sebald, *Annu. Rep. NMR Spectrosc.*, 2000, **41**, 186–264.
51 T. Gullion and J. Schaefer, *J. Magn. Reson.*, 1989, **81**, 196–200.
52 T. G. Oas, R. G. Griffin and M. H. Levitt, *J. Chem. Phys.*, 1988, **89**, 692.
53 R. Tycko and G. Dabbagh, *Chem. Phys. Lett.*, 1990, **173**, 461.
54 Y. K. Lee, N. D. Kurur, M. Helmle, O. G. Johannessen, N. C. Nielsen and M. H. Levitt, *Chem. Phys. Lett.*, 1995, **242**, 304–309.
55 M. Hohwy, H. J. Jakobsen, M. Edén, M. H. Levitt and N. C. Nielsen, *J. Chem. Phys.*, 1998, **108**, 2686–2694.
56 M. Carravetta, M. Edén, A. Brinkmann, X. Zhao and M. H. Levitt, *Chem. Phys. Lett.*, 2000, **321**, 205–215.
57 P. E. Kristiansen, M. Carravetta, W. C. Lai and M. H. Levitt, *Chem. Phys. Lett.*, 2004, **390**, 1–7.
58 P. E. Kristiansen, M. Carravetta, J. D. van Beek, W. C. Lai and M. H. Levitt, *J. Chem. Phys.*, 2006, **124**, 234510–234519.
59 D. H. Brouwer, P. E. Kristiansen, C. A. Fyfe and M. H. Levitt, *J. Am. Chem. Soc.*, 2005, **127**, 542–543.
60 D. H. Brouwer, R. J. Darton, R. E. Morris, C. A. Fyfe and M. H. Levitt, *J. Am. Chem. Soc.*, 2005, **127**, 10365–10370.
61 A. E. Bennett, D. P. Weliky and R. Tycko, *J. Am. Chem. Soc.*, 1998, **120**, 4897–4898.
62 J. Schmedt auf der Günne, *J. Magn. Reson.*, 2003, **165**, 18–32.
63 J. D. van Beek, M. Carravetta, G. C. Antonioli and M. H. Levitt, *J. Chem. Phys.*, 2005, **122**, 244510.
64 D. P. Weitekamp, J. R. Garbow and A. Pines, *J. Chem. Phys.*, 1982, **77**, 2870–2883.
65 J. Baum, M. Munowitz, A. N. Garroway and A. Pines, *J. Chem. Phys.*, 1985, **83**, 2015–2025.
66 J. Baum and A. Pines, *J. Am. Chem. Soc.*, 1986, **108**, 7447–7454.
67 C. E. Hughes, *Prog. Nucl. Magn. Reson. Spectrosc.*, 2004, **45**, 301–313.
68 B. M. Fung, A. K. Khitrin and K. Ermolaev, *J. Magn. Reson.*, 2000, **142**, 97–101.
69 H. Y. Carr and E. M. Purcell, *Phys. Rev.*, 1954, **94**, 630638.
70 S. R. Hartmann and E. L. Hahn, *Phys. Rev.*, 1962, **128**, 2042–2053.
71 A. Pines, M. G. Gibby and J. S. Waugh, *Chem. Phys. Lett.*, 1972, **15**, 373.
72 G. Metz, X. Wu and S. O. Smith, *J. Magn. Reson., Ser. A*, 1994, **110**, 219–227.
73 A. Bielecki and D. P. Burum, *J. Magn. Reson., Ser. A*, 1995, **116**, 215–220.
74 G. Neue and C. Dybowski, *Solid State Nucl. Magn. Reson.*, 1997, **7**, 333–336.
75 J. F. Haw, R. A. Crook and R. C. Crosby, *J. Magn. Reson.*, 1986, **66**, 551.
76 A. J. Horsewill, *Prog. Nucl. Magn. Reson. Spectrosc.*, 1999, **35**, 359–389.
77 S. A. Smith, T. O. Levante, B. H. Meier and R. R. Ernst, *J. Magn. Reson., Ser. A*, 1994, **30**, 75–105.
78 A. M. Gil and E. Alberti, *Solid State Nucl. Magn. Reson.*, 1998, **11**, 203–209.
79 J. M. B. Kellogg, I. I. Rabi, N. F. Ramsey, Jr and J. R. Zacharias, *Phys. Rev.*, 1939, **56**, 728–743.
80 N. F. Ramsey, *Phys. Rev.*, 1940, **58**, 226–236.
81 J. M. Brown and A. Carrington, *Rotational Spectroscopy of Diatomic Molecules*, Cambridge University Press, Cambridge, 2003.
82 C. R. Morcombe and K. W. Zilm, *J. Magn. Reson.*, 2003, **162**, 479–486.
83 A. Abragam, *The Principles of Nuclear Magnetism*, Clarendon Press, Oxford, 1961.
84 J. D. van Beek, *J. Magn. Reson.*, 2007, **187**, 19–26.

